2.3. Down-regulation of HGF mRNA and protein from P7 to P14 is correlated with a reduction in both the rate of c-Met phosphorylation and of OPC numbers in the striatum

To assess whether the regulation of HGF expression is regulated in accordance with oligodendrogenesis, we determined the levels of HGF mRNA by quantitative real-time RT-PCR in the striatum at both P7 and P14. As shown in Fig. 3a, the relative levels of HGF mRNA, standardized to GAPDH mRNA, decreased from P7 to P14. Immunostaining of HGF revealed that HGF IR was detected at low levels in small neurons of the striatum, while HGF IR was detected at relatively high levels in large neurons (Fig. 3b, upper panel, inset) and blood vessels. In contrast, HGF IR was below the detection limit in PDGFRα⁺ OPCs (Fig. 3b, lower panel). In addition, HGF IR was detected in the striatal matrix with a concentration gradient from the outer surface (higher HGF levels) to the inner side (lower levels) of the striatum. The overall levels of HGF IR slightly decreased from P7 to P14. We next assessed whether the regulation of HGF can contribute to

the activation of c-Met by taking advantage of an anti-phospho-c-Met antibody that specifically recognizes the intracellular phosphorylated tyrosine residues (1230, 1234, and 1235) of c-Met, which reflect HGF intracellular signaling. Immunoprecipitation by c-Met and subsequent Western blotting of both phospho-c-Met and c-Met revealed that the ratio of phospho-c-Met per c-Met in the striatum decreased from P7 to P14 (Fig. 3c). Taken together with the finding that OPC numbers decreased from P7 to P14 (Fig. 2a), our findings suggest that the down-regulation of HGF in the striatum correlates with the reduction of both the endogenous activation rate of c-Met and OPC cell numbers from P7 to P14.

2.4. c-Met is tyrosine phosphorylated and thereby activated in OPCs and oligodendrocytes during early postnatal development in vivo

We next examined which cellular population of oligodendrocyte lineage cells was activated by HGF during postnatal development. NG2 IR (red) overlapped with phospho-c-Met IR
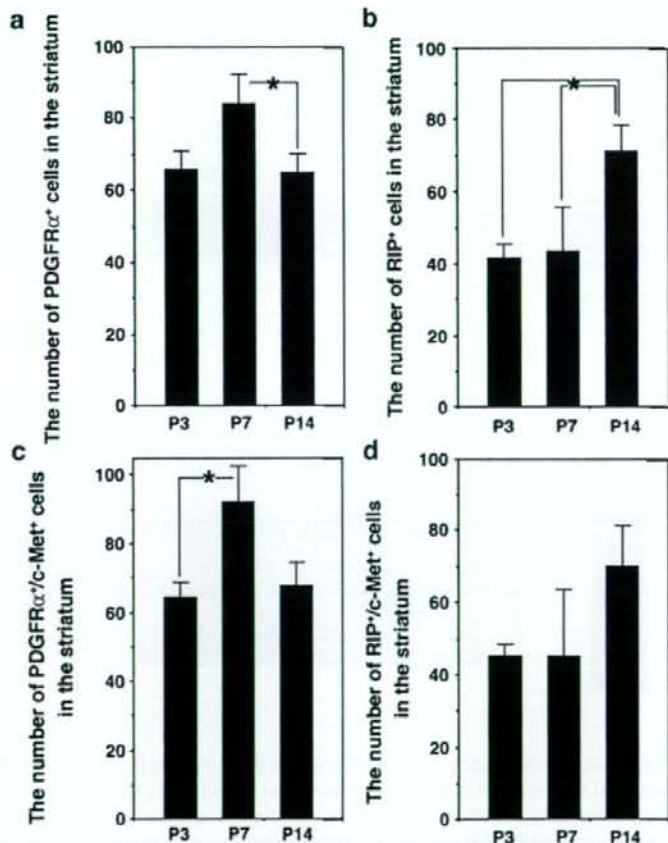

Fig. 2 – The numbers of PDGFRα⁺ OPCs are reciprocally regulated with those of RIP⁺ oligodendrocytes during postnatal development. The numbers of PDGFRα⁺ (n=6) (a), RIP⁺ (n=6) (b), PDGFRα and c-Met double-positive (PDGFRα⁺/c-Met⁺) (n=3) (c) and RIP⁺/c-Met⁺ (n=3) (d) cells within the field of view (FOV, 0.18 mm²; Fig. S2) of the striatum during development are shown. The results are expressed as the mean±SE. *p<0.05.

(green) from P3 to P14 (Figs. 4a–i). PDGFRα IR (red) also overlapped with phospho-c-Met IR (green) (Figs. 4j–l) and RIP IR (red) overlapped with phospho-c-Met IR (green) at P14 (Figs. 4m–o). Elimination of phospho-c-Met IR by pre-absorption of phospho-c-Met antibody with excess amounts of immunogen validated the specificity of the phospho-c-Met antibody (Figs. 4p–r). These findings demonstrated that c-Met, in both OPCs and oligodendrocytes, is in fact physiologically activated in the striatum during early postnatal development.

2.5. Proliferation of OPCs is promoted by intrastriatal treatment with recombinant human HGF

To determine the biological signals transduced by HGF in OPCs and oligodendrocytes, we assessed whether HGF could modulate the proliferation of OPCs and their differentiation into oligodendrocytes by stereotaxic injection of recombinant human HGF (rhHGF) into the left striatum at both P7 and P10 (0.3 or 1.0 μg per animal in each injection; Fig. 5a) and by
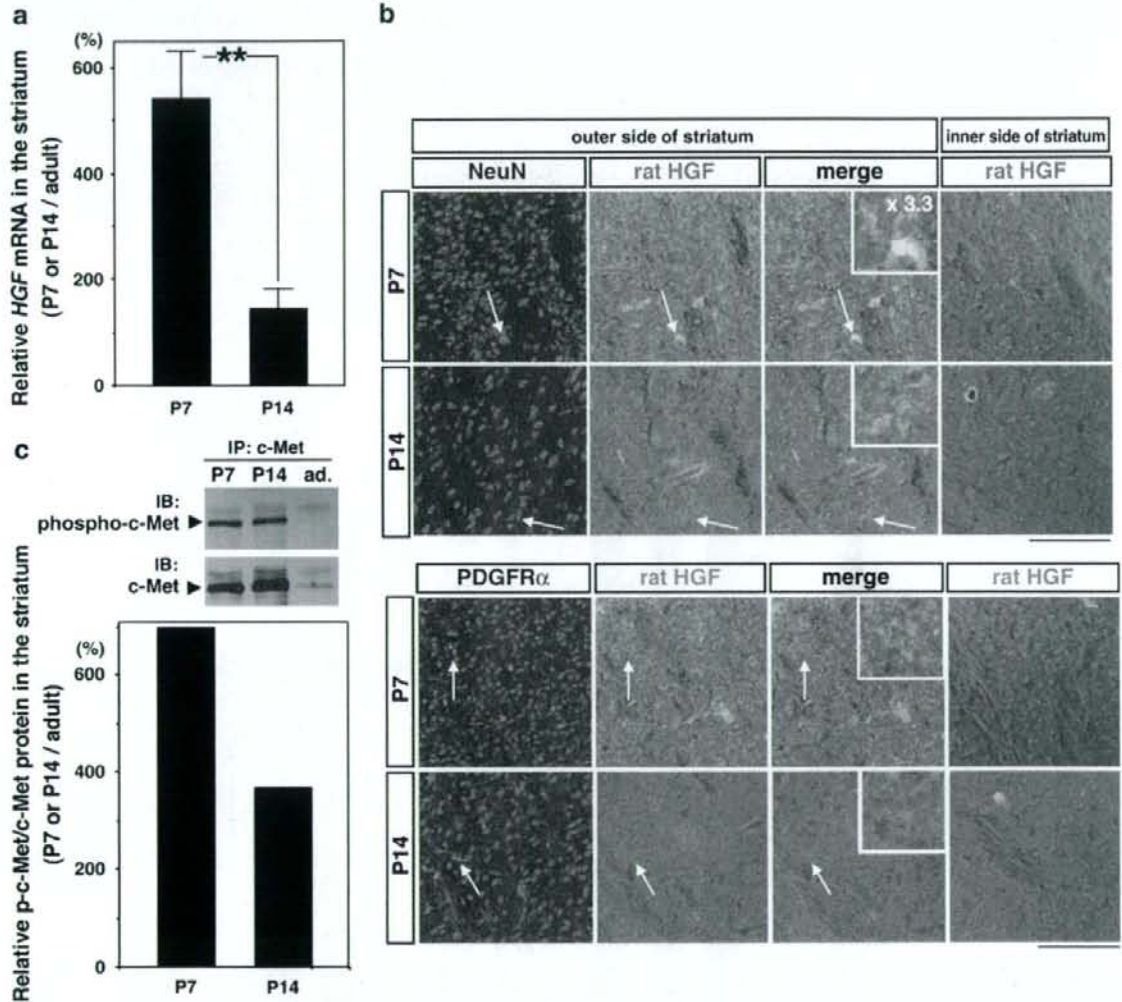

Fig. 3 – Regulation of the expression of HGF mRNA, localization of HGF IR, and phosphorylation of c-Met in the striatum during development. (a) Quantitative real-time RT-PCR of *HGF* in the striatum at P7 and P14 is shown (left panel). *HGF* mRNA levels were standardized to *GAPDH* mRNA. The ratio of *HGF* mRNA levels was expressed relative to those of adult striatum. The results are expressed as the mean ± SE. **$p < 0.01$. (b) Double fluorescence immunostaining of neuronal nuclei (NeuN) and rat HGF (right, upper) or PDGFRα and rat HGF (right, lower) in the striatum. The insets designate higher (×3.3) magnification views, indicated by white arrows. Scale bar = 100 μm. (c) Immunoprecipitation by c-Met and subsequent Western blotting of phospho-c-Met (phospho-Tyr$^{1230/1234/1235}$, p-c-Met) or c-Met during development. Lower panel shows a quantitative graph. The ratio of p-c-Met protein level per c-Met protein at P7 or P14 was expressed relative to those of adult striatum. IP, immunoprecipitation; IB, immunoblotting.

subsequent analysis of NG2+/BrdU+ cells in the striatum at P11. Two injections of PBS served as controls (Fig. 5a). Delivery of rhHGF into the striatum was confirmed in P11 rats by immunostaining using an affinity-purified antibody that was specific for human HGF and does not cross-react with rat HGF (Fig. S2). In PBS-injected control animals, substantial numbers of NG2+/BrdU+ (red/green) cells were evident, indicating the presence of large numbers of proliferating NG2+ OPCs at this
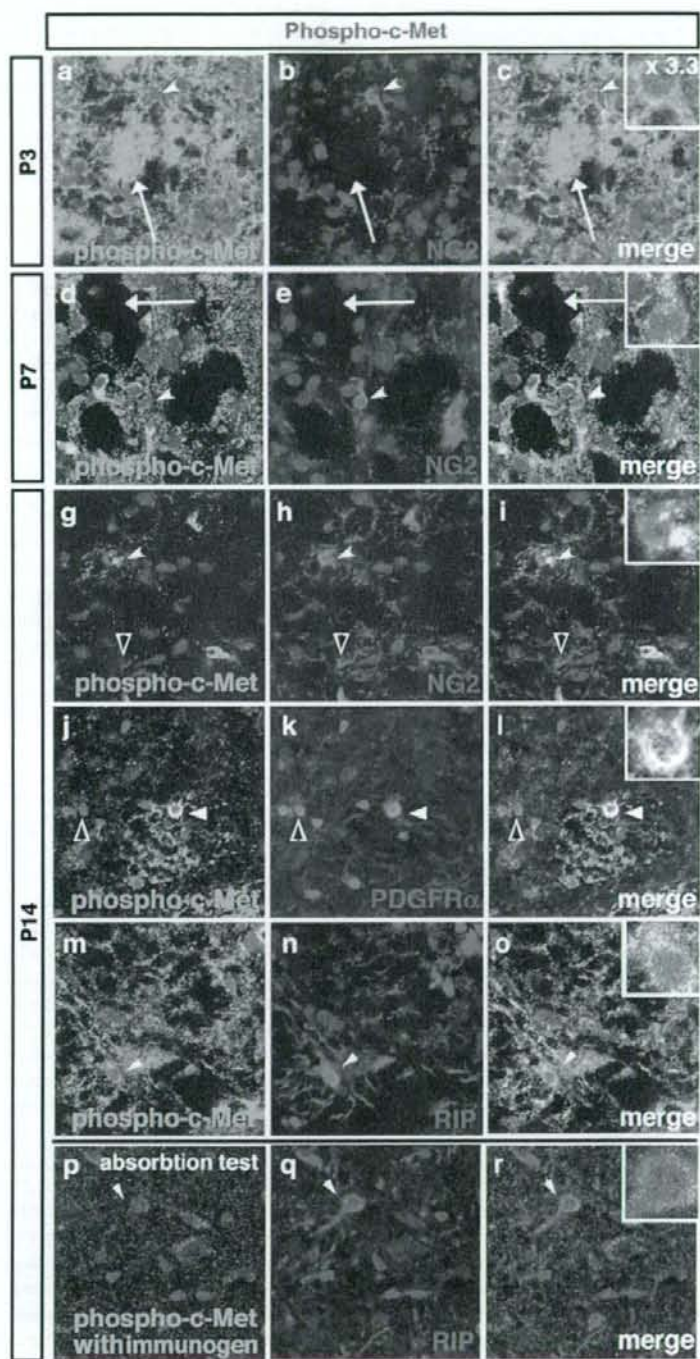
developmental stage in the striatum (Fig. 5b, upper panel, arrows). In HGF-treated animals, larger numbers of BrdU[+]/NG2^{+} OPCs were evident compared with controls (Fig. 5b). The relative ratio (%) of BrdU[+]/NG2^{+} cells per total number of NG2^{+} cells increased to 121% and 139% by intrastriatal treatment with 0.3 µg and 1.0 µg of HGF, respectively, compared with PBS treatment (Fig. 5c, and Table 1, upper panel) as revealed by quantitative analysis in the striatum (see details in Experimental procedures; Fig. S2). These findings suggested that OPC proliferation was increased by HGF in the striatum. To further confirm the role of HGF in OPCs, we analyzed effects on the corpus callosum (white matter tissue) since larger numbers of OPCs are present in the corpus callosum compared with the striatum and phospho-c-Met IR is present physiologically in NG2^{+} OPCs of the corpus callosum during development (Fig. 5d, e and Fig. S1). When rhHGF was injected into the striatum, we detected human HGF IR in the corpus callosum (Fig. S2). Double fluorescence immunostaining of both BrdU and NG2 revealed that the relative ratio (%) of BrdU[+]/NG2^{+} cells per total number of NG2^{+} cells increased to 141% by HGF (1.0 µg) treatment compared with PBS treatment in the corpus callosum (Table 1, lower panel). Therefore, HGF promoted the proliferation of NG2^{+} OPCs in both the striatum and corpus callosum.

2.6. The extent of OPC differentiation into MBP[+] oligodendrocytes is slightly diminished by HGF treatment but is slightly increased by anti-HGF IgG treatment

We next assessed whether HGF could modulate OPC differentiation into oligodendrocytes by stereotaxic injection of rhHGF into the left striatum at both P7 and P10 (0.3 or 1.0 µg per animal in each injection; Fig. 6a) and by subsequent analysis of the numbers of MBP[+]/BrdU^{+} cells at P11 (Fig. 6a). Two injections of PBS served as controls. In PBS-injected control animals, substantial numbers of MBP[+]/BrdU[+] (red/green) cells were evident, indicating the presence of large numbers of newly formed MBP[+] oligodendrocytes at this developmental stage (Fig. 6b, upper panel). In HGF-treated animals, smaller numbers of BrdU[+]/MBP[+] oligodendrocytes were evident compared with PBS-treated animals (Fig. 6b). The relative number of BrdU[+]/MBP^{+} cells decreased to 65% and 69%, by intrastriatal treatment with 0.3 µg and 1.0 µg of HGF, respectively (Fig. 6c), as revealed by quantitative analysis (see details in Experimental procedures; Fig. S2). In contrast, injection of anti-HGF "functional blocking" antibody increased the relative numbers of BrdU[+]/MBP^{+} cells. These findings suggest that de novo formation of oligodendrocytes was decreased by HGF but increased by anti-HGF IgG. Therefore, it seems most likely that HGF contributes to the attenuation of endogenous and exogenous differentiation of OPCs into oligodendrocytes in the striatum.

2.7. Western blot analysis of MBP reveals a reduction in MBP protein levels after treatment with HGF

To further assess the role of HGF in the modulation of MBP protein levels, Western blot analysis was performed in striatal tissues using the same injection protocol as described for Fig. 5 without BrdU (Fig. 7a). The average level of MBP protein, standardized to GAPDH protein in the striatum, decreased to 42% compared with controls after treatment with HGF (Figs. 7b, c).

2.8. HGF reduces the levels of MBP[+] myelin sheaths in the striatum

To determine whether the reduced levels of MBP protein in the striatum is associated with the reduced myelination of MBP[+] oligodendrocytes, animals were treated with either HGF or PBS using the same injection protocol as described in Fig. 7a, and the levels of MBP[+] myelin sheaths were quantified in the striatum at P14 (4 days after the last treatment), according to the method described by Butt and Dinsdale (2005b) with slight modification (see details in Experimental procedures). Briefly, the numbers of MBP[+] myelin sheaths were quantified using a grid of 20×20 points to yield a total of 400 points within the field of view (FOV) (3850 µm²), and a myelin index was calculated as the percentage of points intersected by a myelin sheath. MBP IR in the HGF-treated group was lower than the PBS-treated group (Figs. 8a, b). These findings suggested that the levels of MBP[+] myelin sheaths decreased in the striatum after HGF treatment.

2.9. Striatal myelination is attenuated by HGF treatment

To examine the effects of HGF on myelination at the ultra-structural level, we treated animals with either rhHGF or PBS at both P7 and P10 using the same injection protocol as described in Fig. 7a. Coronal sections of the P14 rat striatum were analyzed using a HITACHI electron microscope. Fig. 9 shows representative views. In PBS-treated animals, mature myelinated axons were largely evident, while in HGF-treated animals, the numbers of myelinated axons markedly decreased. It seems unlikely that the attenuation of myelination by HGF is caused by HGF activity on neurites since immunostaining and Western blot analysis of the neurite marker, neurofilament200 (NF200), revealed that intrastriatal HGF treatment did not reduce neuritogenesis in the striatum (Figs. S3a, b). These findings suggest that HGF has an inhibitory effect on the differentiation and maturation of oligodendrocytes.

Fig. 4 – Phospho-c-Met IR is present in NG2^{+} OPCs from P3 to P14 and in RIP[+] oligodendrocytes at P14. Double fluorescence immunostaining for phospho-c-Met (green) and NG2 (red) (a–i), for phospho-c-Met (green) and PDGFRα (red) (j–l), or for phospho-c-Met (green) and RIP (red) (m–o), counterstained with TOPRO-3 iodide (blue) in P3 (a–c), P7 (d–f), and P14 (g–r) rat striatum. Arrowheads indicate double-immunostained cells with NG2/phospho-c-Met (a–i), PDGFRα/phospho-c-Met (j–l), or RIP/phospho-c-Met (m–o). Bottom panel (p–r) shows the immunostaining for phospho-c-Met that is pre-absorbed with excess amounts of immunogen. Arrows indicate the positions of the bundles of innervating nerve fibers and their growth cones. The insets designate higher (×3.3) magnification views, indicated by white arrowheads. Black arrowheads indicate NG2 (red) or PDGFRα (red) single-positive cells. Scale bar = 100 µm.

3.   Discussion

Here we provided the first evidence that c-Met and tyrosine phosphorylated, and thereby activated c-Met are highly evident in both NG2$^+$ (PDGFRα^+) OPCs and RIP$^+$ oligodendrocytes from P3 to P14 in vivo, suggesting a role for HGF in these cells. Furthermore, we also provided evidence that HGF promotes the proliferation of NG2$^+$ OPCs in vivo by double immunohistochemical analyses of NG2$^+$/BrdU$^+$ cells after intrastriatal treatment with HGF at both P7 and P10, immediately after the critical point of the switch of the notch signals from Jagged1/notch/HES-1 to contactin/notch/Deltex1. This is consistent with the previous in vitro finding that HGF promotes OPC proliferation (Yan and Rivkees, 2002), suggesting that it might result from a direct action of HGF on OPCs. In addition, we found that HGF could inhibit both the differentiation of NG2$^+$ OPCs and the myelination of oligodendrocytes.

Although a precise molecular mechanism of this HGF effect is unclear, it has been shown that HGF has the ability to induce HES-1 mRNA production in MDA-MB-435-β4 cells and that the activation of notch leads to c-Met inhibition by the binding of HES-1 to the *c-met* promoter (Stella et al., 2005). Additionally, cultured bone marrow cells in the presence of HGF express both notch and Jagged1 on day 3 (Okumoto et al., 2003), suggesting a link between the HGF-c-Met signal and the notch
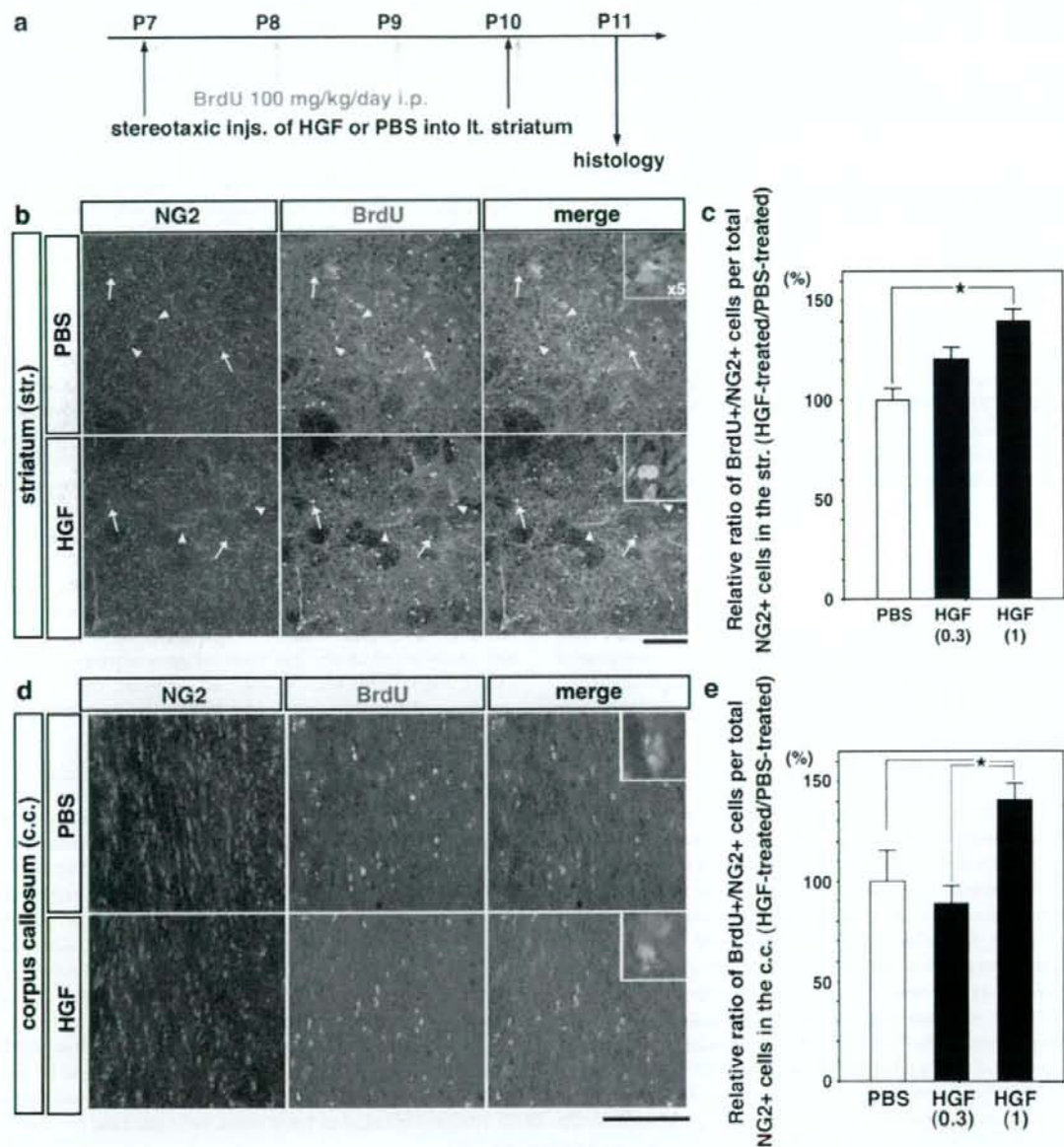
Table 1 – Relative values of BrdU[+] and/or NG2^{+} cells in the striatum and corpus callosum after HGF or PBS treatment

	PBS	HGF 0.3 µg	HGF 1 µg	HGF 0.3 µg/PBS (%)	HGF 1 µg/PBS (%)
Striatum					
BrdU^{+} cells (a)	101.7±7.0	116.8±7.0	127.0±2.6	114.9±6.9	124.9±2.6
NG2^{+} cells (b)	88.0±8.5	104.0±3.4	100.0±4.1	118.2±7.7	113.6±4.7
BrdU[+]/NG2^{+} cells (c)	26.3±3.8	37.8±2.3*	42.0±0.8*	143.4±8.5*	159.5±3.1*
Ratio of c/a (%)	26.0±2.5%	32.5±2.1%	33.5±1.3%	125.0±8.0	128.8±5.1
Ratio of c/b (%)	30.7±1.7%	37.0±1.7%	42.8±1.9%*	120.7±5.6	139.4±6.3*
Corpus Callosum					
BrdU^{+} cells (a)	45.8±4.2	52.5±2.2	57.2±7.0	114.6±4.8	124.9±15.3
NG2^{+} cells (b)	97.8±9.3	107.7±12.1	100.2±9.7	110.1±12.4	102.5±9.9
BrdU[+]/NG2^{+} cells (c)	27.8±1.6	28.7±6.2	41.7±5.9	103.2±22.3	150.0±21.2
Ratio of c/a (%)	61.1±2.1%	53.9±9.4%	72.5±2.7%	88.2±15.4	118.7±4.4
Ratio of c/b (%)	29.3±4.6%	26.0±2.6%	41.2±2.3%*	88.7±8.9	140.6±7.8*

The absolute cell number in the FOV (0.18 mm²) of P11 striatum or the FOV (0.045 mm²) of P11 corpus callosum (Fig. S2) that had been treated with PBS or HGF was expressed as mean±SE (*p<0.05).
a, the absolute number of BrdU^{+} cells in the FOV.
b, the absolute number of NG2^{+} cells in the FOV.
c, the absolute number of BrdU[+]NG2^{+} cells in the FOV.

pathway in certain types of cells. It is postulated that HGF may have the capability to induce notch signaling, presumably via a HES-1 signal in OPCs. Hence, HGF may favor proliferation of NG2^{+} OPCs but can also inhibit the differentiation of OPCs into mature oligodendrocytes even after P6.

Alternatively, it remains possible that the HGF-c-Met signals function independently of the notch signals in these processes. Colognato et al. (2004) reported a working model of the cooperation of growth factor and integrin signaling pathways. The PDGFRα-αVβ3 integrin complex induces proliferation, while axonal contact induces laminine2 binding to the α6β1 integrin complex with ErbB2/4 and, in turn, enhances survival, differentiation, and myelin formation (Colognato et al., 2004). Therefore, the modulation of such signaling pathways by HGF might be an alternative molecular mechanism. The promotion of OPC proliferation and the inhibition of its differentiation into mature myelinating oligodendrocytes may permit neurite outgrowth in the striatum at this developmental stage. The promotion of OPC differentiation into mature oligodendrocytes may lead to the presentation of myelin inhibitory proteins that inhibit axon outgrowth, such as NOGO-A/NI-220, myelin-associated glycoprotein (MAG), and oligodendrocyte-myelin glycoprotein (OMgp), on the

mature oligodendrocyte cell surface (Chen et al., 2000; McKerracher and Winton, 2002). In addition, it should be noted that NG2^{+} glial cells have been shown to provide a favorable substrate on which to grow axons (Yang et al., 2006). Indeed, this developmental stage is important for neurite outgrowth in the striatum. In the rat nigrostriatal dopaminergic system, as in all rat striatal areas where dopaminergic innervation rapidly increases from P4 to P6 (Burke, 2003; Voorn et al., 1988), higher levels of HGF mRNA might be beneficial for both OPC proliferation and inhibition of OPC differentiation to permit neurite outgrowth in a developmental stage-dependent manner. The reduction of HGF mRNA levels from P7 to P14 may permit OPC differentiation into myelinating oligodendrocytes. HGF may also play a role in differentiated oligodendrocytes; the clarification of this role is the next important issue to be examined.

In summary, we provided the first evidence that the c-Met/HGF receptor is activated in OPCs and oligodendrocytes during postnatal development and that HGF promotes the proliferation of OPCs and attenuates their differentiation into myelinating oligodendrocytes in the rat striatum. Our findings suggest a role for the HGF-c-Met system in oligodendrocyte development in concert with neuritogenesis.

Fig. 5 – NG2^{+} OPC proliferation is promoted by HGF treatment in both the striatum and corpus callosum during development. (a) The schematic illustration of the experimental protocol. Either rhHGF (0.3 or 1.0 µg per injection) or PBS was stereotaxically injected into the left striatum at both P7 and P10. BrdU (100 mg/kg) was intraperitoneally injected daily from P7 to P10. The animals were sacrificed at P11 for histological analyses. (b) Double immunostaining for NG2 and BrdU in the striatum of P11 rats that were treated with either PBS (upper panel) or rhHGF (lower panel) (1.0 µg per injection) at both P7 and P10. Arrows indicate NG2^{+} OPCs. Arrowheads indicate NG2^{+} blood vessels. Insets are the higher (×5) magnification views. Scale bar=100 µm. (c) A quantitative graph of the relative ratio of BrdU[+]/NG2^{+} cells per total number of NG2^{+} cells in the striatum. The results are expressed as the mean±SE and tested for significance with ANOVA and Scheffe's post hoc tests (*p<0.05). The average ratio of BrdU[+]/NG2^{+} cells per total number of NG2 cells in the striatum of PBS-treated rats was defined as 100%. (d) Double immunostaining for NG2 and BrdU in the corpus callosum of P11 rats that were treated with either PBS (upper panel) or rhHGF (lower panel) (1.0 µg per injection) at both P7 and P10. Scale bar=100 µm. (e) A quantitative graph of the relative ratio of BrdU[+]/NG2^{+} cells per total number of NG2^{+} cells in the corpus callosum. The results are expressed as the mean±SE and tested for significance with ANOVA and Scheffe's post hoc tests (*p<0.05). The average ratio of BrdU[+]/NG2^{+} cells per total number of NG2 cells in the corpus callosum of PBS-treated rats was defined as 100%.

4. Experimental procedures

4.1. Recombinant human HGF and anti-HGF IgG

Recombinant human HGF (rhHGF) was purified from the conditioned medium of Chinese hamster ovary cells that were transfected with an expression vector containing human HGF cDNA as described earlier (Nakamura et al., 1989; Seki et al., 1990). The purity of the rhHGF was greater than 98% as determined by SDS–PAGE. Anti-rat HGF antibody was raised in rabbits after immunization of animals with recombinant rat HGF and the IgG fraction was purified using protein A-Sepharose (Pharmacia Biotech, Uppsala, Sweden), as previously described (Ohmichi et al., 1998). This anti-rat

HGF antibody does not cross-react with human HGF. One microgram of anti-rat HGF IgG neutralizes the biological activity of at least 5 ng rat HGF.

4.2. Animals

Timed-pregnant Sprague–Dawley (SD) rats were purchased from SLC (Shizuoka, Japan) and were housed in individual cages in a temperature-controlled room under a 12-h light/12-h dark cycle. The acquisition, care, housing, use, and disposition of animals were in compliance with institutional laws and regulations of the Osaka University Graduate School of Medicine. All efforts were made to minimize animal discomfort and the number of animals used. For developmental analysis, we used SD rat pups of the following developmental time
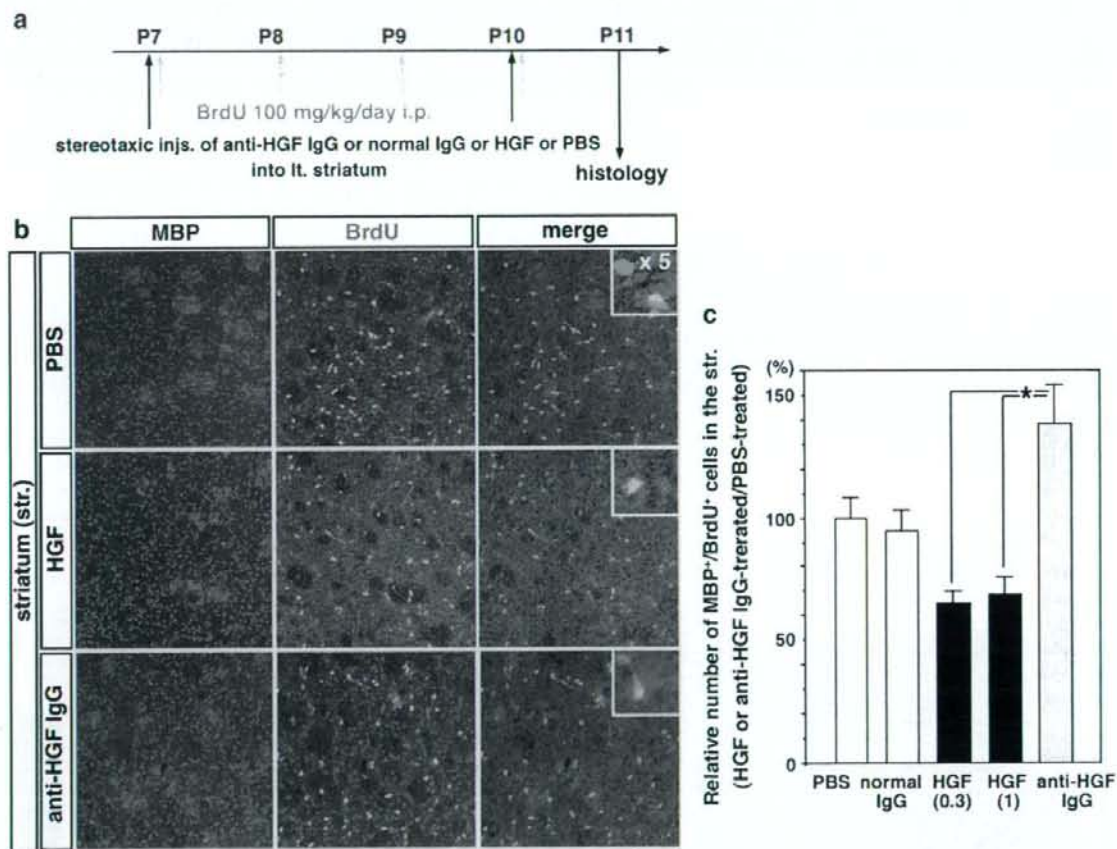

Fig. 6 – Differentiation of OPCs into MBP⁺ oligodendrocytes is slightly diminished by HGF treatment and slightly increased by anti-HGF IgG treatment. (a) The schematic illustration of the experimental protocol. rhHGF (0.3 or 1.0 μg per injection), anti-HGF "functional blocking" IgG, normal IgG, or PBS was stereotaxically injected into the left striatum at both P7 and P10. BrdU (100 mg/kg) was intraperitoneally injected daily from P7 to P10. The animals were sacrificed at P11 for histological analyses. (b) Double immunostaining for MBP and BrdU in the striatum of P11 rats that were treated with PBS (upper panel), rhHGF (middle panel) (1.0 μg per injection), or anti-HGF IgG (lower panel) at both P7 and P10. Insets are the higher (×5) magnification views. Scale bar=100 μm. (c) A quantitative graph of MBP⁺/BrdU⁺ cell numbers. The results are expressed as the mean±SE and tested for significance with ANOVA and Scheffe's post hoc tests (*$p<0.05$). The average MBP⁺/BrdU⁺ cell number of PBS-treated rats was defined as 100%.
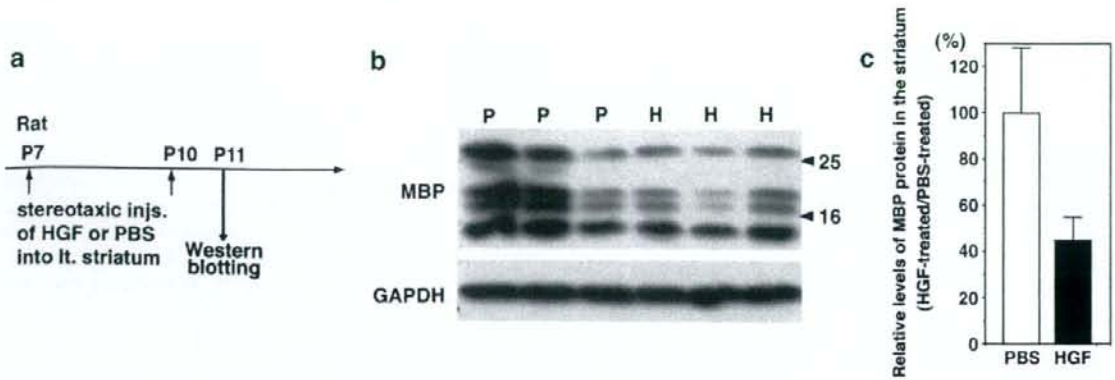
Fig. 7 – HGF reduces MBP protein levels in the striatum. (a) The schematic illustration of the experimental protocol. Either rhHGF (1.0 μg per injection) or PBS was stereotaxically injected into the left striatum at both P7 and P10. The animals were sacrificed at P11 for Western blot analysis. (b) Western blotting for MBP and GAPDH in the striatum of P11 rats that were treated with either PBS (P) or rhHGF (H). Arrowheads indicate molecular marker sizes. (c) Relative MBP protein levels were quantified and expressed as the mean ± SE. The relative mean level of MBP to GAPDH proteins in the PBS-treated group was defined as 100%.

points: P3, P7, P11, P14, and postnatal week 8 (8w). To assess the role of HGF in striatal oligodendrogenesis, each SD rat that was injected with rhHGF was paired with a littermate that received injections of PBS on the same day. For injections, rats were anesthetized by intraperitoneal injection of 30 mg/kg ketamine and 5 mg/kg xylazine. The skull was placed in a stereotaxic apparatus and a 1.5-mm hole was created in the cranium. The stereotaxic coordinates for injections into the striatum were 0 mm caudal to bregma, 2.5 mm lateral to the midline, and 4.0 mm below the surface of the skull (Sherwood, 1970). Using a 30-gauge needle (Hamilton, Reno, NV) and a 10-μL Hamilton microsyringe, 0.3 μg or 1.0 μg rhHGF (1.5 or 0.5 μg/μL in PBS) (n=4 each), 10 μg anti-rat HGF IgG (5 μg/μL in PBS) (n=4), normal rabbit IgG (5 μg/μL in PBS) (n=3), or PBS (n=3) were stereotaxically injected into the striatum at 0.25 μL/min. After injection, the needle was left in place for 5 min to prevent reflux and

slowly withdrawn in several steps over 5 min. Three days after the injection (i.e., at P10), animals were re-injected with the same liquid into the same coordinates. The animals were sacrificed under deep anesthesia for both Western blotting at P11 and immunohistochemical analyses at either P11 or P14. For BrdU incorporation, BrdU (100 mg/kg, Nacalai Tesque, Kyoto, Japan) was intraperitoneally injected daily for 4 days from P7 to P10.

4.3.   Tissue preparation

Animals at P3, P7, P11, or P14 were transcardially perfused with ice-cold PBS followed by ice-cold 4% paraformaldehyde (PFA) in PBS under deep anesthesia. The brains were excised and immersed in the same fixative for 1.5 h at 4 °C and the striatum was dissected prior to immunohistochemistry. Fixed
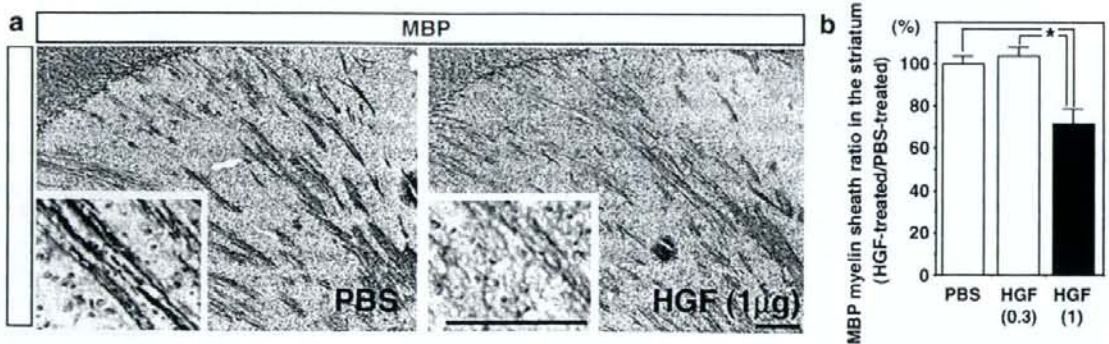

Fig. 8 – HGF reduces the number of MBP+ myelin sheaths in the striatum. (a) Immunostaining for MBP in the left striatum at P14 in animals treated with PBS (left panel) or rhHGF (right panel) (1.0 μg per injection) at both P7 and P10 using the same injection protocol described for Fig. 7a. Scale bar=100 μm. (b) The quantitative numbers of MBP+ myelin sheaths in the HGF-treated and PBS-treated striata are shown. The relative mean number of MBP+ myelin sheaths in the PBS-treated group was defined as 100%. The results are expressed as the mean ± SE and tested for significance with ANOVA and Scheffe's post hoc tests (*p<0.05).
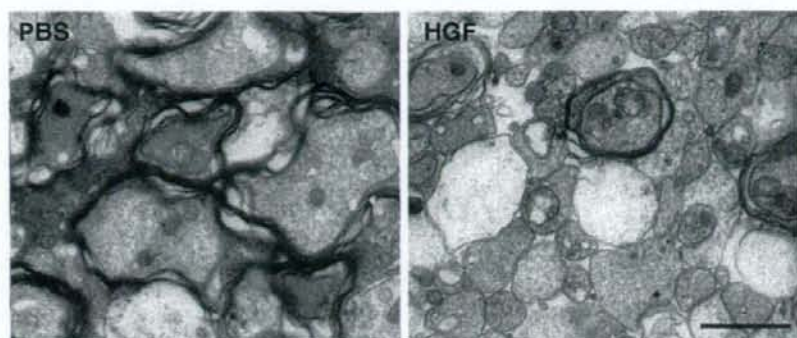
Fig. 9 – Ultrastructural examination by electron microscopy reveals the reduction of myelinated axon numbers by HGF intrastriatal treatment. Representative electron micrographs of coronal sections of the striatum at P14 in animals that were treated with either PBS (left panel) or HGF (right panel) (1.0 µg per injection) using the same injection protocol as described in Fig. 7a are shown. In the HGF-treated group, thick myelinated axons were rarely observed compared with those in the PBS-treated group. Scale bar=0.8 µm.

tissues were immersed in 20% sucrose in PBS overnight at 4 °C, frozen in CO_2, and cut into either 20-µm thick transverse or longitudinal sections using a cryostat.

4.4. Immunohistochemistry

Cryosections were incubated in blocking buffer consisting of 5% normal goat serum (S26-100 mL, CHEMICON, CA) and 0.3% Triton X-100 in PBS for 30 min at room temperature (RT) followed by one of the following primary antibodies for 1.5 h at RT: (1) rabbit polyclonal anti-c-Met antibody (1:100; sc-162, Santa Cruz, CA); (2) rabbit polyclonal anti-phospho-c-Met antibody (phospho-Tyr$^{1230/1234/1235}$, 1:100; QCB44-888, Bio-source-Invitrogen, CA); (3) rabbit polyclonal anti-MBP antibody (1:100; 01417, Stem Cell Technologies, USA); (4) mouse mono-clonal anti-NG2 antibody (1:100; MAB5384, CHEMICON); (5) mouse monoclonal anti-RIP antibody (1:10000; MAB1580, CHEMICON); (6) affinity-purified rabbit polyclonal anti-human HGF antibody (1:100) (Yamada et al., 1995); (7) rabbit polyclonal anti-PDGFRα antibody (1:500, kindly provided by Dr. W.B. Stallcup); and (8) goat polyclonal anti-PDGFRα antibody (1:20, AF1062, R&D, Minneapolis). Specificity of rabbit and goat anti-PDGFRα antibodies was confirmed by double immunostaining of these antibodies as presented in Fig. S4. Immunolabeling was visualized by either fluorescence or diaminobenzidine (DAB) immunostaining. For fluorescence immunostaining, sections were incubated with secondary antibodies conjugated with either Alexa488 or Alexa546 (1:600; Invitrogen) and TOPRO-3 iodide (1:1000; Invitrogen) for nuclear staining in blocking buffer for 20 min at RT, washed with PBS, mounted with Crystal mount (Biomeda, CA), and observed under an LSM 5 PASCAL confocal microscope (ZEISS, Germany). For DAB immunostaining, sections were treated with 3% hydrogen peroxide for 5 min to quench endogenous peroxidases prior to the first antibody reaction. The sections were then incubated with primary antibody in blocking buffer for 1.5 h at RT. After washing with PBS, sections were incubated with Envision+ System Labeled Polymer-HRP anti-mouse or anti-rabbit (Dako-Cytomation, CA) as the second antibody for 30 min at RT,

stained with DAB (0.05%), counterstained with Mayer's hema-toxylin (WAKO, Japan), washed with PBS, and mounted with EUKITT (O. Kinder, Germany). The images were captured using an Olympus System Microscope BX51 (Tokyo, Japan).

4.5. BrdU incorporation

Cryosections were treated with acetone for 10 s, air-dried, washed with PBS, and incubated with 2 N HCl for 30 min at RT. After incubation with blocking buffer, sections were incubated overnight at 4 °C with rat monoclonal anti-BrdU antibody (1:100; OBT0030, Oxford Biotech. Ltd., UK), and then with either mouse monoclonal anti-NG2 antibody (1:100; MAB5384, CHE-MICON) or rabbit polyclonal anti-MBP antibody (1:100; 01417, Stem Cell Technology) in blocking buffer and washed with PBS. The sections were incubated with secondary antibodies, conjugated with either Alexa488 or Alexa546 (1:600; Invitro-gen), and then with TOPRO-3 iodide (1:1,000; Invitrogen) for nuclear staining. Specimens were observed under an LSM 5 PASCAL confocal microscope.

4.6. Electron microscopy

P14 rats were transcardially perfused with 2% PFA and 2% glutaraldehyde in PBS under deep anesthesia. The brains were excised and immersed in the same fixative overnight. Tissue blocks were post-fixed in 2% osmium tetroxide in PBS for 2 h at 4 °C, dehydrated through an ethanol gradient, and embedded in Epon. Ultrathin sections (90 nm) were cut with an ultramicrotome (Ultracut, Reichert-Jung) and stained with 4% uranyl acetate for 20 min at RT and with 1% Pb for 10 min at RT prior to examination by electron microscopy (H-7100, HITACHI, Japan).

4.7. Immunoprecipitation and Western blotting

Striatal lysates were prepared from the P7, P14, and 8-week-old rats in lysis buffer [50 mM Tris–HCl (pH 7.5), 150 mM NaCl, 1% Triton X-100, 10% glycerol, 25 mM β-glycerophosphate, 50 mM

NaF, 2 mM Na_3VO_4, 1 mM PMSF, 4 µg/mL antipain, 1 µg/mL pepstatin A, 3 µg/mL leupeptin, and 2 µg/mL aprotinin] using a Mixer Mill 300 (QIAGEN). The lysates were pre-adsorbed with 20 µL protein G-Sepharose (GE Healthcare) for 2 h at 4 °C and centrifuged to remove protein G-Sepharose; equal amounts of supernatants (6.4 mg protein) were incubated overnight at 4 °C with 6.4 µL mouse anti-c-Met (1:1000, B2, Santa Cruz) antibody and 20 µL protein G-Sepharose beads. Protein G-Sepharose beads were washed three times with lysis buffer and dissolved in SDS–PAGE sample buffer. The immunoprecipitates were separated by 7.5% SDS–PAGE under reduced conditions, electroblotted onto a polyvinylidene difluoride membrane (Bio-Rad), and probed with rabbit anti-phospho-c-Met (phospho-$Tyr^{1230/1234/1235}$, 1:500; QCB44-888, Biosource-Invitrogen) or rabbit anti-c-Met (1:1000; sc-162, Santa Cruz) antibody. Proteins reacting with these antibodies were detected using ECL+ enhanced chemiluminescence (Amersham Pharmacia Biotech). Densitometric quantification of the scanned band intensities, corresponding to phospho-c-Met and c-Met in P3, P7, and 8w samples, was performed via digitizing each band by densitometry using Image J software on a Macintosh computer and were further normalized based on the intensity of c-Met.

The striatal lysates were prepared in TNE buffer (150 mM NaCl, 5 mM EDTA, 1% NP40, and 2 mM Tris–HCl, pH 7.5) using a Mixer Mill 300 (QIAGEN) after two hemi-intrastriatal injections of either HGF (1.0 µg per injection) or PBS into P11 rats. Equal amounts of lysates (20 µg) were resolved by 12% SDS–PAGE under reducing conditions and then immunoblotted with either rabbit anti-MBP (1:1000; 01417, Stem Cell Technologies) or mouse monoclonal anti-NF200 (1:1500, N0142, Sigma) antibody. GAPDH served as an internal control. An enhanced chemiluminescence system was used for visualization and captured on X-ray film. Densitometric quantification of the scanned band intensities, corresponding to MBP and NF200 in both the HGF-treated ($n=3$) and PBS-treated ($n=3$) samples, was performed via digitizing each band by densitometry using Image J software on a Macintosh computer and were further normalized based on the intensity of GAPDH.

4.8. RNA purification and quantitative real-time RT-PCR

Total RNA was prepared from microdissected striatal tissues of P7 and P14 rats, as well as from adult rats, using an RNeasy Micro Kit (QIAGEN) according to the manufacturer's instructions. For quantitative real-time RT-PCR, 2.0 µg of each RNA was reverse transcribed using SuperScript II (Invitrogen) according to the manufacturer's instructions. Real-time RT-PCR was carried out with an ABI PRISM 7900 sequence detection system (Applied Biosystems) to quantify relative levels of mRNA in the samples as described previously (Nakamura et al., 2006). For amplification of rat HGF and GAPDH (the endogenous control) genes, both the Universal PCR master mix (Applied Biosystems) and Taq-Man MGB probes (FAM dye-labeled) were used (rat HGF exons 17–18, Rn00566673m1; rodent GAPDH TaqMan VIC Probe; Applied Biosystems). All standards and samples were assayed in duplicate. Thermal cycling was initiated with an initial denaturation at 50 °C for 2 min and 95 °C for 10 min, followed by 40 cycles of PCR (95 °C for 15 s; 60 °C for 1 min). HGF mRNA levels

were standardized to GAPDH mRNA. The ratio of HGF mRNA levels was expressed relative to that of adult striatum. Results were expressed as means ± SE of the number of observations. Statistical significance was assessed by ANOVA and Scheffe's post hoc test. A level of $p < 0.05$ was considered significant. Significance was determined after three separate experiments.

4.9. Quantitative analysis

Cell counts of OPCs were done in the P3 ($n=3$), P7 ($n=3$), and P11 ($n=3$) rat striatum. A single FOV (0.18 mm^2) was analyzed in the center of the sagittal view of the striatum under a 20× objective and 3 FOVs were averaged. The numbers of $PDGFR\alpha^+$ cells, $PDGFR\alpha^+$ and $NG2^+$ cells, and $PDGFR\alpha^+$ and $c-Met^+$ cells were quantified. Results were expressed as means ± SE and were tested for significance using ANOVA and Fisher's post hoc test. Cell counts and the levels of OPC proliferation were determined according to the method described by Butt and Dinsdale (2005b) with slight modification. Briefly, cell counts were done in P11 rat striatum that was treated with PBS ($n=3$), 0.3 µg rhHGF ($n=4$), or 1.0 µg rhHGF ($n=4$). A single FOV (0.18 mm^2) was analyzed and averaged in four FOVs (Fig. S2b) in the coronal view of the striatum under a 20× objective to yield a total area of 0.72 mm^2; the numbers of $BrdU^+$ and $NG2^+$ cells were quantified. A single FOV (0.045 mm^2) was analyzed and averaged in two FOVs (Fig. S2b) in the coronal view of the corpus callosum under a 20× objective and the numbers of $BrdU^+$ and $NG2^+$ cells were quantified. Results were expressed as means ± SE and were tested for significance using ANOVA and Fisher's post hoc test. A single FOV (0.72 mm^2) was analyzed and averaged in two FOVs (Fig. S2c) under a 10× objective to yield a total area of 1.48 mm^2 and the numbers of $BrdU^+$ and MBP^+ cells were quantified. Results were expressed as means ± SE and were tested for significance using ANOVA and Scheffe's post hoc test. The extent of myelination was quantified in MBP-immunostained, sagittal, striatal sections of P14 rats that were treated with PBS ($n=6$), 0.3 µg HGF ($n=3$), or 1.0 µg HGF ($n=4$) using a grid of 20 × 20 points to yield a total area of 400 points within the single FOV (3850 μm^2); a myelin index (ratio) was determined as the percentage of points intersected by a myelin sheath (at least two out of four transects). The number of neurites was quantified in NF200-immunostained, sagittal, striatal sections. A single FOV (1.54 mm^2) in the rostral area of striatum was quantified using NIH image. The average myelin index in the rostral striatum of P14 rats that were treated with PBS was defined as 100%. Identical regions were selected as those described in Fig. S2; results were expressed as means ± SE and were tested for significance using ANOVA and Tukey–Kramer's post hoc test for myelin index and Fisher's post hoc test for relative levels of NF200 IR.

Appendix A. Supplementary data

Supplementary data associated with this article can be found, in the online version, at doi:10.1016/j.brainres.2007.02.045.

REFERENCES

Bladt, F., Riethmacher, D., Isenmann, S., Aguzzi, A., Birchmeier, C., 1995. Essential role for the c-met receptor in the migration of myogenic precursor cells into the limb bud. Nature 376, 768–771.

Bogler, O., Wren, D., Barnett, S.C., Land, H., Noble, M., 1990. Cooperation between two growth factors promotes extended self-renewal and inhibits differentiation of oligodendrocyte-type-2 astrocyte (O-2A) progenitor cells. Proc. Natl. Acad. Sci. U. S. A. 87, 6368–6372.

Burke, R.E., 2003. Postnatal developmental programmed cell death in dopamine neurons. Ann. N.Y. Acad. Sci. 991, 69–79.

Butt, A.M., Dinsdale, J., 2005a. Fibroblast growth factor 2 mediated disruption of myelin-forming oligodendrocytes in vivo is associated with increased tau immunoreactivity. Neurosci. Lett. 375, 28–32.

Butt, A.M., Dinsdale, J., 2005b. Opposing actions of fibroblast growth factor-2 on early and late oligodendrocyte lineage cells in vivo. J. Neuroimmunol. 166, 75–87.

Chen, M.S., Huber, A.B., van der Haar, M.E., Frank, M., Schnell, L., Spillmann, A.A., Christ, F., Schwab, M.E., 2000. Nogo-A is a myelin-associated neurite outgrowth inhibitor and an antigen for monoclonal antibody IN-1. Nature 403, 434–439.

Colognato, H., Ramachandrappa, S., Olsen, I.M., French-Constant, C., 2004. Integrins direct Src family kinases to regulate distinct phases of oligodendrocyte development. J. Cell Biol. 167, 365–375.

Ebens, A., Brose, K., Leonardo, E.D., Hanson Jr., M.G., Bladt, F., Birchmeier, C., Barres, B.A., Tessier-Lavigne, M., 1996. Hepatocyte growth factor/scatter factor is an axonal chemoattractant and a neurotrophic factor for spinal motor neurons. Neuron 17, 1157–1172.

Funakoshi, H., Nakamura, T., 2001. Identification of HGF-like protein as a novel neurotrophic factor for avian dorsal root ganglion sensory neurons. Biochem. Biophys. Res. Commun. 283, 606–612.

Funakoshi, H., Nakamura, T., 2003. Hepatocyte growth factor: from diagnosis to clinical applications. Clin. Chim. Acta 327, 1–23.

Hamanoue, M., Takemoto, N., Matsumoto, K., Nakamura, T., Nakajima, K., Kohsaka, S., 1996. Neurotrophic effect of hepatocyte growth factor on central nervous system neurons in vitro. J. Neurosci. Res. 43, 554–564.

Hayashi, Y., Kawazoe, Y., Sakamoto, T., Ojima, M., Wang, W., Takazawa, T., Miyazawa, D., Ohya, W., Funakoshi, H., Nakamura, T., Watabe, K., 2006. Adenoviral gene transfer of hepatocyte growth factor prevents death of injured adult motoneurons after peripheral nerve avulsion. Brain Res. 1111, 187–195.

Honda, S., Kagoshima, M., Wanaka, A., Tohyama, M., Matsumoto, K., Nakamura, T., 1995. Localization and functional coupling of HGF and c-Met/HGF receptor in rat brain: implication as neurotrophic factor. Brain Res. Mol. Brain Res. 32, 197–210.

Hu, Q.D., Ang, B.T., Karsak, M., Hu, W.P., Cui, X.Y., Duka, T., Takeda, Y., Chia, W., Sankar, N., Ng, Y.K., Ling, E.A., Maciag, T.,

Small, D., Trifonova, R., Kopan, R., Okano, H., Nakafuku, M., Chiba, S., Hirai, H., Aster, J.C., Schachner, M., Pallen, C.J., Watanabe, K., Xiao, Z.C., 2003. F3/contactin acts as a functional ligand for Notch during oligodendrocyte maturation. Cell 115, 163–175.

Hu, Q.D., Ma, Q.H., Gennarini, G., Xiao, Z.C., 2006. Cross-talk between F3/contactin and Notch at axoglial interface: a role in oligodendrocyte development. Dev. Neurosci. 28, 25–33.

Ishihara, N., Takagi, N., Niimura, M., Takagi, K., Nakano, M., Tanonaka, K., Funakoshi, H., Matsumoto, K., Nakamura, T., Takeo, S., 2005. Inhibition of apoptosis-inducing factor translocation is involved in protective effects of hepatocyte growth factor against excitotoxic cell death in cultured hippocampal neurons. J Neurochem. 95, 1277–1286.

Isogawa, K., Akiyoshi, J., Kodama, K., Matsushita, H., Tsutsumi, T., Funakoshi, H., Nakamura, T., 2005. Anxiolytic effect of hepatocyte growth factor infused into rat brain. Neuropsychobiology 51, 34–38.

Kato, S., Funakoshi, H., Nakamura, T., Kato, M., Nakano, I., Hirano, A., Ohama, E., 2003. Expression of hepatocyte growth factor and c-Met in the anterior horn cells of the spinal cord in the patients with amyotrophic lateral sclerosis (ALS): immunohistochemical studies on sporadic ALS and familial ALS with superoxide dismutase 1 gene mutation. Acta Neuropathol. (Berl) 106, 112–120.

Maina, F., Hilton, M.C., Ponzetto, C., Davies, A.M., Klein, R., 1997. Met receptor signaling is required for sensory nerve development and HGF promotes axonal growth and survival of sensory neurons. Genes Dev. 11, 3341–3350.

Maina, F., Hilton, M.C., Andres, R., Wyatt, S., Klein, R., Davies, A.M., 1998. Multiple roles for hepatocyte growth factor in sympathetic neuron development. Neuron 20, 835–846.

McKerracher, L., Winton, M.J., 2002. Nogo on the go. Neuron 36, 345–348.

McKinnon, R.D., Matsui, T., Dubois-Dalcq, M., Aaronson, S.A., 1990. FGF modulates the PDGF-driven pathway of oligodendrocyte development. Neuron 5, 603–614.

Miyazawa, T., Matsumoto, K., Ohmichi, H., Katoh, H., Yamashima, T., Nakamura, T., 1998. Protection of hippocampal neurons from ischemia-induced delayed neuronal death by hepatocyte growth factor: a novel neurotrophic factor. J. Cereb. Blood Flow Metab. 18, 345–348.

Nakamura, T., Nawa, K., Ichihara, A., 1984. Partial purification and characterization of hepatocyte growth factor from serum of hepatectomized rats. Biochem. Biophys. Res. Commun. 122, 1450–1459.

Nakamura, T., Nishizawa, T., Hagiya, M., Seki, T., Shimonishi, M., Sugimura, A., Tashiro, K., Shimizu, S., 1989. Molecular cloning and expression of human hepatocyte growth factor. Nature 342, 440–443.

Nakamura, K., Ohya, W., Funakoshi, H., Sakaguchi, G., Kato, A., Takeda, M., Kudo, T., Nakamura, T., 2006. Possible role of scavenger receptor SRCL in the clearance of amyloid-betain Alzheimer's disease. J. Neurosci. Res. 84, 874–890.

Nishiyama, A., Lin, X.H., Giese, N., Heldin, C.H., Stallcup, W.B., 1996. Co-localization of NG2 proteoglycan and PDGF alpha-receptor on O2A progenitor cells in the developing rat brain. J. Neurosci. Res. 43, 299–314.

Ohmichi, H., Koshimizu, U., Matsumoto, K., Nakamura, T., 1998. Hepatocyte growth factor (HGF) acts as a mesenchyme-derived morphogenic factor during fetal lung development. Development 125, 1315–1324.

Okumoto, K., Saito, T., Hattori, E., Ito, J.I., Adachi, T., Takeda, T., Sugahara, K., Watanabe, H., Saito, K., Togashi, H., Kawata, S., 2003. Differentiation of bone marrow cells into cells that express liver-specific genes in vitro: implication of the Notch signals in differentiation. Biochem. Biophys. Res. Commun. 304, 691–695.

Okura, Y., Arimoto, H., Tanuma, N., Matsumoto, K., Nakamura, T.,

Yamashima, T., Miyazawa, T., Matsumoto, Y., 1999. Analysis of neurotrophic effects of hepatocyte growth factor in the adult hypoglossal nerve axotomy model. Eur. J. Neurosci. 11, 4139–4144.

Powell, E.M., Mars, W.M., Levitt, P., 2001. Hepatocyte growth factor/ scatter factor is a mitogen for interneurons migrating from the ventral to dorsal telencephalon. Neuron 30, 79–89.

Schmidt, C., Bladt, F., Goedecke, S., Brinkmann, V., Zschiesche, W., Sharpe, M., Gherardi, E., Birchmeier, C., 1995. Scatter factor/ hepatocyte growth factor is essential for liver development. Nature 373, 699–702.

Seki, T., Ihara, I., Sugimura, A., Shimonishi, M., Nishizawa, T., Asami, O., Hagiya, M., Nakamura, T., Shimizu, S., 1990. Isolation and expression of cDNA for different forms of hepatocyte growth factor from human leukocyte. Biochem. Biophys. Res. Commun. 172, 321–327.

Sherwood, N.M., 1970. Stereotaxic Atlas of Developing Rat Brain. University of California Press Berkeley, Los Angeles, London.

Stella, M.C., Trusolino, L., Pennacchietti, S., Comoglio, P.M., 2005. Negative feedback regulation of Met-dependent invasive growth by Notch. Mol. Cell Biol. 25, 3982–3996.

Sun, W., Funakoshi, H., Nakamura, T., 2002a. Localization and functional role of hepatocyte growth factor (HGF) and its receptor c-met in the rat developing cerebral cortex. Brain Res. Mol. Brain Res. 103, 36–48.

Sun, W., Funakoshi, H., Nakamura, T., 2002b. Overexpression of HGF retards disease progression and prolongs life span in a transgenic mouse model of ALS. J. Neurosci. 22, 6537–6548.

Uehara, Y., Minowa, O., Mori, C., Shiota, K., Kuno, J., Noda, T., Kitamura, N., 1995. Placental defect and embryonic lethality in mice lacking hepatocyte growth factor/scatter factor. Nature 373, 702–705.

Voorn, P., Kalsbeek, A., Jorritsma-Byham, B., Groenewegen, H.J., 1988. The pre- and postnatal development of the dopaminergic cell groups in the ventral mesencephalon and the dopaminergic innervation of the striatum of the rat. Neuroscience 25, 857–887.

Wang, S., Sdrulla, A.D., diSibio, G., Bush, G., Nofziger, D., Hicks, C., Weinmaster, G., Barres, B.A., 1998. Notch receptor activation inhibits oligodendrocyte differentiation. Neuron 21, 63–75.

Yamada, A., Matsumoto, K., Iwanari, H., Sekiguchi, K., Kawata, S., Matsuzawa, Y., Nakamura, T., 1995. Rapid and sensitive enzyme-linked immunosorbent assay for measurement of HGF in rat and human tissues. Biomed. Res. 16, 105–114.

Yamamoto, Y., Livet, J., Pollock, R.A., Garces, A., Arce, V., deLapeyriere, O., Henderson, C.E., 1997. Hepatocyte growth factor (HGF/SF) is a muscle-derived survival factor for a subpopulation of embryonic motoneurons. Development 124, 2903–2913.

Yan, H., Rivkees, S.A., 2002. Hepatocyte growth factor stimulates the proliferation and migration of oligodendrocyte precursor cells. J. Neurosci. Res. 69, 597–606.

Yang, Z., Suzuki, R., Daniels, S.B., Brunquell, C.B., Sala, C.J., Nishiyama, A., 2006. NG2 glial cells provide a favorable substrate for growing axons. J. Neurosci. 26, 3829–3839.

Zhang, L., Himi, T., Morita, I., Murota, S., 2000. Hepatocyte growth factor protects cultured rat cerebellar granule neurons from apoptosis via the phosphatidylinositol-3 kinase/Akt pathway. J. Neurosci. Res. 59, 489–496.

Amyotrophic lateral sclerosis models and human neuropathology: similarities and differences

Shinsuke Kato

Abstract Amyotrophic lateral sclerosis (ALS) is a progressive neurodegenerative disease that primarily involves the motor neuron system. The author initially summarizes the principal features of human ALS neuropathology, and subsequently describes in detail ALS animal models mainly from the viewpoint of pathological similarities and differences. ALS animal models in this review include strains of rodents that are transgenic for superoxide dismutase 1 (SOD1), ALS2 knockout mice, and mice that are transgenic for cytoskeletal abnormalities. Although the neuropathological results obtained from human ALS autopsy cases are valuable and important, almost all of such cases represent only the terminal stage. This makes it difficult to clarify how and why ALS motor neurons are impaired at each clinical stage from disease onset to death, and as a consequence, human autopsy cases alone yield little insight into potential therapies for ALS. Although ALS animal models cannot replicate human ALS, in order to compensate for the shortcomings of studies using human ALS autopsy samples, researchers must inevitably rely on ALS animal models that can yield very important information for clarifying the pathogenesis of ALS in humans and for the establishment of reliable therapy. Of course, human ALS and all ALS animal models share one most important similarity in that both exhibit motor neuron degeneration/death. This important point of similarity has shed much light on the pathomechanisms of the motor neuron degeneration/death at the cellular and molecular levels that would not have been appreciated if only human ALS autopsy samples had

been available. On the basis of the aspects covered in this review, it can be concluded that ALS animal models can yield very important information for clarifying the pathogenesis of ALS in humans and for the establishment of reliable therapy only in combination with detailed neuropathological data obtained from human ALS autopsy cases.

Keywords Amyotrophic lateral sclerosis ·
Animal models · Superoxide dismutase 1 ·
Transgenic rodents · Human pathology

Introduction

Amyotrophic lateral sclerosis (ALS) in humans is a progressive disease characterized by degeneration of both upper and lower motor neurons. Upper motor neurons are located mainly in layer V of the motor cortex, and are known as Betz cells, which are giant cells approximately 60–120 μm in diameter. Cytoarchitecturally, the axons of the upper motor neurons connect directly with the lower motor neurons located in the motor nuclei of the brainstem and the anterior horn of the spinal cord. The axons of the lower motor neurons project mainly to skeletal muscles. Although an essential pathological feature of ALS is motor neuron loss, affected motor neurons often contain characteristic inclusions in the perikarya, dendrites and axons. The concept of "ALS" has been widely debated for over 130 years since Charcot first introduced the term "la sclérose latérale amyotrophique" in 1874 [15]. Currently, in the era of advanced genetics, the molecular bases and mechanisms of ALS are now known to be very complex, thus explaining the different phenotypes of ALS. Therefore, ALS is considered to be a type of syndrome rather than a single disease entity.

S. Kato (✉)
Department of Neuropathology,
Institute of Neurological Sciences, Faculty of Medicine,
Tottori University, Nishi-cho 36-1, Yonago 683-8504, Japan
e-mail: kato@grape.med.tottori-u.ac.jp

◯ Springer

Human pathologists are entirely dependent on human ALS autopsy samples in order to acquire a more definitive understanding of the etiology and pathogenesis of ALS motor neuron death. As almost all ALS autopsy samples are obtained from patients at the terminal stage, it is difficult to clarify how and why ALS motor neurons are impaired at each clinical stage from disease onset to death. Therefore, analyses of ALS autopsy samples alone is not sufficient to lead to possible therapies for ALS. Under these circumstances, many researchers including pathologists have come to rely on animal models of ALS in order to gain insights into both the mechanisms involved in motor neuron death and possible therapeutic approaches. Inevitably, these ALS animal models have different characteristics, because even human ALS, which is the prototype for these models, is not a single disease. On the basis of the aspects covered in this review, however, the author wish to emphasize that ALS animal models can yield very important information for clarifying the pathogenesis of ALS in humans only in combination with detailed neuropathological data obtained from human ALS autopsy cases.

Human ALS neuropathology

Sporadic ALS (SALS)

Human ALS is classified into two major subtypes: sporadic ALS (SALS) and familial ALS (FALS). In SALS, the degenerative change is mainly restricted to the motor neuron system, except for the oculomotor, trochlear and abducens nuclei controlling eye movements, as well as Onufrowicz's nucleus which functions in fecal and urinary continence. Upper motor neurons such as the Betz cells in the motor cortex are also affected. Degeneration of the corticospinal tracts in the anterior and lateral columns of the spinal cord are particularly evident. Especially, the corticospinal tract degeneration is most evident in the lower spinal cord segment, supporting the hypothesis of a dying back degeneration of axons. In the degenerated primary motor tracts, there is loss of large myelinated fibers in association with variable astrocytic gliosis. Destruction of these fibers is usually associated with the appearance of lipid-laden macrophages.

An essential histopathological feature of SALS is loss of both upper and lower motor neurons, especially large anterior horn cells throughout the length of the spinal cord. In addition, striated muscles demonstrate denervation atrophy, i.e., neurogenic muscle atrophy. The surviving motor neurons often show histopathological features including cytoplasmic shrinkage and lipofuscin granules. The cytopathology of the affected motor neurons in SALS is characterized by the following two important intracytoplasmic inclusions.

Bunina bodies

Bunina bodies are small eosinophilic granular inclusions (1–3 μm in diameter) in the anterior horn cells, appearing either singly or in a group, and sometimes arranged in small beaded chains. These Bunina bodies are observed within the cytoplasm or dendrites (Fig. 1a), but they have not been found within the axoplasm. Bunina bodies stain bright red with hematoxylin and eosin (H&E) staining, deep blue with phosphotungstic acid hematoxylin, and blue with Luxol fast blue. Immunohistochemical studies have revealed that they express only cystatin C (Fig. 1b), and do not have a variety of other immunoreactive epitopes such as ubiquitin. Ultrastructurally, Bunina bodies consist of electron-dense amorphous material that contains tubules or vesicular structures. The amorphous material frequently includes a cytoplasmic island containing neurofilaments and other micro-organelles [58].

These specific bodies were originally described by a Russian pathologist Bunina [12] in 1962 in two FALS patients belonging to two different families. After Bunina's report, Hirano immediately confirmed that these inclusion bodies were present in a number of ALS patients, including those with SALS and FALS neuropathologically identical to SALS, as well as Guamanian ALS [41]. Although not all ALS patients necessarily have Bunina bodies histologically, Bunina bodies themselves are currently considered a specific histopathological hallmark of ALS. Broadly speaking, Bunina bodies can be observed in SALS, frontotemporal lobar degeneration with motor neuron disease (FTLD-MND; terminologically identical to ALS with dementia, ALSD), mutant SOD1-unlinked FALS that is neuropathologically identical to SALS, and Guamanian ALS. However, there have been no reports that Bunina bodies are present in SOD1-mutated FALS (Table 1) or transgenic rodents with mutant SOD1.

Skein-like inclusions (SLIs) and round hyaline inclusions (RHIs)

The SLIs are intracytoplasmic filamentous structures [58] that are frequently encountered in preparations immunostained for ubiquitin, although in H&E preparations they are hardly visible or sometimes detected as faintly eosinophilic structures. SLIs form essential aggregates of thread-like structures. In more aggregated forms, SLIs show dense collections of filaments, in which the SLIs appear as spherical structures. RHIs are pale eosinophilic inclusions with halos in the remaining anterior horn cells in H&E preparations [57]. Sometimes, they lack halos and have irregular margins associated with filamentous structures similar to SLIs. Immunohistochemically, SLIs and RHIs are positive for ubiquitin, but negative for phosphorylated
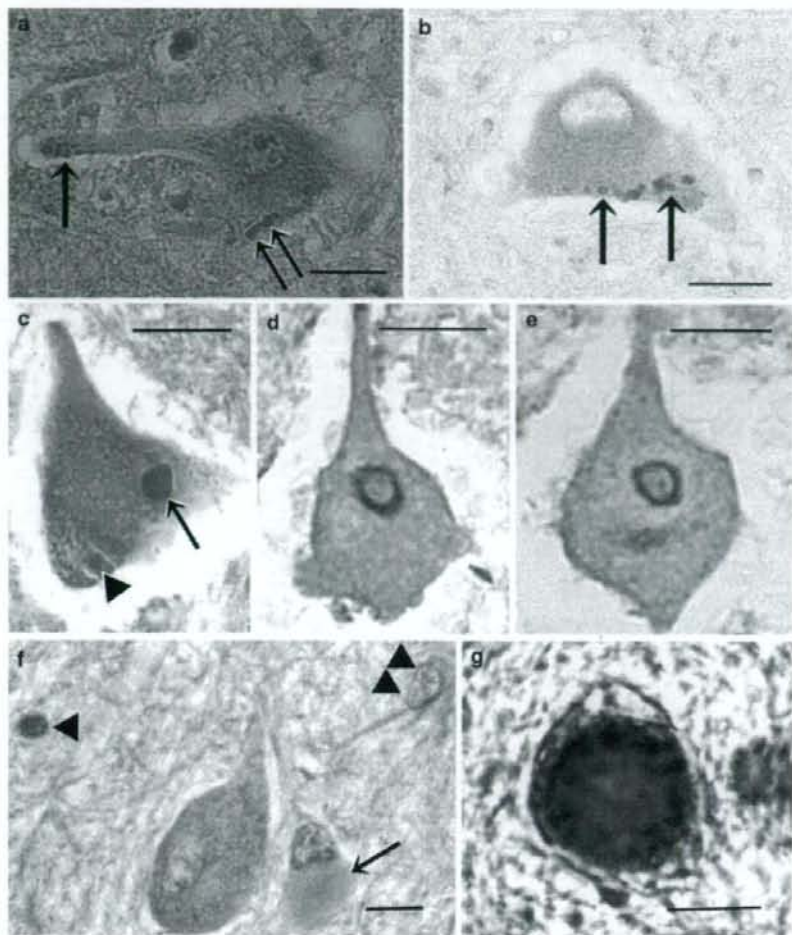
Fig. 1 Neuropathological findings of human ALS. **a, b** Light micrographs of Bunina bodies. **a** Bunina bodies in an anterior horn cell of an SALS patient. Bunina bodies are small eosinophilic inclusions (approximately 1–3 μm in diameter) and staining bright red with H&E. Bunina bodies are observed within the cytoplasm (*double arrows*), being arranged in a chain-like formation. In addition, Bunina bodies are also seen within the dendrites (*arrow*), appearing as a cluster. H&E. **b** Cystatin C immunostaining. Bunina bodies are positive for cystatin C (*double arrows*). A Bunina body (indicated by the *center arrow*) appears as a round structure with central-lucent core, which corresponds to a cytoplasmic island containing neurofilaments and other microorgans at the ultrastructural level. **c–e** Light micrographs of neuronal Lewy-body-like hyaline inclusions (LBHIs). **c** A round LBHI (*arrow*) is observed in the cytoplasm of the anterior horn cell. This round LBHI is composed of eosinophilic core with paler peripheral halo. A small ill-defined LBHI (*arrowhead*) is also seen in the cytoplasm of the ante-

rior horn cell, and consists of obscure slightly eosinophilic materials. H&E. **d, e** Serial sections of a neuronal LBHI in a spinal anterior horn cell immunostained with the antibodies against SOD1 (**d**) and ubiquitin (**e**). An intraneuronal LBHI is clearly labeled by the antibodies to SOD1 and ubiquitin. The immunoreactivity for both SOD1 and ubiquitin is almost restricted to the halo of the LBHI. **f** Light micrograph of an astrocytic hyaline inclusion (Ast-HI) in the spinal cord anterior horn. The Ast-HI (*arrow*) is round and eosinophilic. The astrocyte-bearing the Ast-HI is morphologically different from the adjacent neuron. The nucleus of the cell bearing the Ast-HI resembles that of a reactive astrocyte (*double arrowheads*) and not the nucleus of an oligodendrocyte (*arrowhead*). H&E. **g** A neurofilamentous conglomerate inclusion showing intense immunohistochemical positivity for phosphorylated neurofilament protein. Scale bar **a** (also for **b–e, g**) 30 μm, Scale bar **f** 10 μm

(p) neurofilament protein (NFP; pNFP) and SOD1 [58]. Ultrastructurally, the essential abnormal filaments of the SLIs range in width from approximately 15 nm in the

naked parts without granules to about 20 nm in parts with fuzzy granules (i.e., fibrils with granules); these fibrils with granules often form bundles. In more aggregated

Table 1 Summary of main neuropathological findings in autopsied patients with familial amyotrophic lateral sclerosis (FALS) with characteristic mutations of superoxide dismutase 1 (SOD1)

SOD1 mutation	Number of patients	Neuronal inclusion	SOD1 aggregation	Bunina body	Corticospinal tract involvement	Posterior column involvement	References
A4V	3	LBHI	+	−	+(slight)	+	[89]
	5	ICI	ND	ND	±(mild)	+(asymmetry)	[18]
A4T	1	LBHI	+	−	+(mild)	+	[92]
G37R	1	LBHI	+	−	+	+	[46]
H43R	1	LBHI	+	−	+	+	[67]
H46R	1	LBHI	+	−	+(very mild)	+(very mild)	[76]
H48Q	1	LBHI&SLI	−	−	+(mild)	minimal	[88]
E100G	1	SLI	−	ND	+	+	[44]
D101N	2	ICHI	ND	ND	−	−	[14]
D101Y	1	LBHI	+	−	+(very mild)	−	[94]
L106V	2	LBHI	+	−	+	+	(Unpublished data from author)
C111Y	1	LBHI	+	−	+	Minimal	[32]
I113T	1	NFT (Brain and brain stem)	ND	ND	+	−	[78]
	1	ICAI	ND	ND	−	ND	[85]
	1	ICAI	+	−	ND	ND	[60]
	1	HC	ND	ND	+	+	[45]
	1	NFCI	−	−	+(slight)	+	[51]
L126S	1	LBHI	+	−	+	+	[93]
2-bp del	2	LBHI	+	−	+(slight/marked)	+	[53]
(L126dellTT)	1	LBHI	+	−	+	−	[50]
C146R	2	LBHI	+	−	+(slight)	+	[71]
Wild type	2	SLI/RHI	−	+	+	−	(Unpublished data from author)

As controls, FALS siblings with wild-type SOD1 are also tabulated in the bottom row

+, present; −, absent

ND not described; *LBHI* Lewy-body-like hyaline inclusion; *ICI* intracytoplasmic inclusion; *SLI* skein-like inclusion; *RHI* round hyaline inclusion; *ICHI* intracytoplasmic hyaline inclusion; *NFT* neurofibrillary tangle (straight filament); *ICAI* intracytoplasmic argyrophilic inclusion (neurofilament accumulation); *HC* hyaline conglomerate (with neurofilament epitope); *NFCI* neurofilamentous conglomerate inclusion; *bp*, base pair; *del* deletion

forms, SLIs that appear to be spherical structures are composed of many bundles of these fibrils with granules [58]. Ultrastructurally, the essential abnormal filaments of the RHIs range in width from approximately 15 nm in the naked parts without granules to about 20 nm in the parts with fuzzy granules (fibrils with granules), being very similar to the fibrils with granules in SLIs [58]. As a whole, RHIs form spherical aggregates without a limiting membrane, and a hypothesis that SLIs evolve to RHIs has even been proposed [58]. Unlike Lewy body-like hyaline inclusions (LBHIs) in mutant SOD1-linked motor neurons, although RHIs are similar to LBHIs in H&E preparations, RHIs are negative for SOD1 [58]. Simply and clearly to state, SLIs/RHIs are ultrastructurally composed of 15–20-nm fibrils with granules, and LBHIs comprised of 15–25-nm granule-coated fibrils with SOD1 epitope [58] (see "Neuronal LBHIs and Ast-HIs").

Familial ALS (FALS)

The FALS accounts for approximately 5–10% of all cases of ALS, and is histopathologically subclassified into two types. One type of FALS is neuropathologically identical to SALS, and frequently contains Bunina bodies. On the basis of the author's observations of two mutant SOD1-unlinked siblings with FALS, this mutant SOD1-non-linked FALS type has similar neuropathological features including Bunina bodies and SLIs/RHIs (Table 1). It is likely that the inclusion bodies originally described by Bunina (Bunina bodies) would have been present in this FALS type. The other form of FALS is that showing posterior column involvement. In addition to the pathological features of SALS, this form also shows degeneration of the middle zone of the posterior column, Clarke nuclei and posterior spinocerebellar tracts. In 1967, Hirano et al. [42] reported

the presence of Lewy body-like hyaline inclusions (LBHIs) in the anterior horn cells throughout the spinal cord in this type of FALS (Fig. 1c). This led to the establishment of this entity as FALS with posterior column involvement. In H&E preparations, neuronal LBHIs show an eosinophilic core with a paler peripheral halo, and their name is derived from their H&E staining features, which resemble those of Lewy bodies in patients with Parkinson's disease.

To date, more than 100 different mutations within all exons of the SOD1 gene and its introns have been identified as being involved in the development of chromosome 21q-linked FALS. These SOD1 gene mutations are present in about 20% of FALS patients. SOD1-mutated FALS shows a variety of clinical phenotypes according to which type of SOD1 gene mutation is responsible: the disease onset and duration are reported to be closely linked to the type of the SOD1 mutation (Fig. 2), i.e., as Fig. 2 demonstrates, FALS with mutant G93A SOD1 shows rapid disease progression with severe neurological symptoms (about 1 year to at most 4 years), while FALS with mutant H46R SOD1 has a very long disease duration with mild neurological signs (11–24 years). From the viewpoint of only the copy number of the mutant SOD1 gene, almost all FALS patients with het-erozygosity for the mutant SOD1 gene carry only a single copy of mutant SOD1 gene, i.e., most patients with SOD1-mutated FALS have the same transgene copy number. Based on this notion, it might be expected that FALS patients with heterozygosity for the mutant SOD1 gene would exhibit a similar expression level of mutant SOD1 protein. However, the protein expression level of mutant SOD1 in FALS patients differs due to the difference in sta-bility of the mutant SOD1 protein itself; FALS patients with unstable-type mutant SOD1 show a lower protein expression level than FALS patients with stable-type mutant SOD1 [86].

Neuropathologically, it is of note that many SOD1-mutated FALS cases are of the posterior column involve-ment type with neuronal LBHIs (Table 1). In addition to neuronal LBHIs, certain long-surviving FALS patients with SOD1 gene mutations show astrocytic hyaline inclusions (Ast-HIs), which were first reported by the author in 1996 [53] (Fig. 1f). Neuronal LBHIs and Ast-HIs are characteris-tic intracytoplasmic structures in SOD1-mutated cells. By marked contrast, Bunina bodies have not been described in mutant SOD1-linked FALS unlike mutant SOD1-unlinked FALS with Bunina bodies (Table 1).

Neuronal LBHIs and Ast-HIs

Neuronal LBHIs and Ast-HIs in SOD1-mutated FALS have strong SOD1 immunoreactivity (Fig. 1d), and both type of inclusion are strongly positive for ubiquitin (Fig. 1e). Inter-estingly, LBHIs/Ast-HIs contain both wild-type and mutant

SOD1 protein [11]. Ultrastructurally, neuronal LBHIs, which consist of filaments and granular materials, exhibit dense cores with rough peripheral halos and lacking a limit-ing membrane. The filaments of these inclusions are com-posed of approximately 15–25-nm granule-coated fibrils in association with normal 10-nm neurofilaments [53–57]. The neurofilaments are located mainly in the periphery and rarely in the central portion. Ast-HIs appear as globular structures that are well demarcated from other cytoplasmic structures, and have no limiting membrane. Ast-HIs are composed of about 15–25-nm granule-coated fibrils with granular materials, sometimes surrounded by normal glial filaments [53–57]. The essential constituents common to both neuronal LBHIs and Ast-HIs are granule-coated fibrils, and the indirect immunogold technique shows label-ing with colloidal gold particles for wild-type and mutant SOD1 only on the surface of the granule-coated fibrils: the essential common constituents of LBHIs/Ast-HIs are SOD1-positive granule-coated fibrils [57].

Another characteristic pathological feature of patients with SOD1-mutated FALS is slight or mild corticospinal tract involvement, in contrast to severe degeneration of the lower motor neurons (Table 1). In patients with FALS lacking LBHI with the I113T mutation, neurofilament pathology is an almost universal feature. Frequently, neurofilamentous conglomerate inclusions (NFCIs) are evi-dent, while they are less common in patients with SALS (less than 5%). Although NFCIs are recognized as homoge-neous, faintly eosinophilic, oval or multi-lobulated inclu-sions in H&E preparations, they are intensely positive for pNFP immunohistochemically (Fig. 1g). Two FALS sib-lings with wild-type SOD1 in the bottom row of Table 1 show Bunina bodies and SLIs/RHIs that are usually observed in SALS, and neuropathologically they showed histology that was almost identical to SALS. These two mutant SOD1-unlinked FALS siblings did not exhibit LBHIs or posterior column degeneration. Although SLIs are seen in SALS and mutant SOD1-unlinked FALS as well as FALS with H48Q and E100G, many cases of SOD1-mutated FALS do not show SLIs (Table 1).

Transgenic animal models linked to superoxide dismutase 1 (SOD1)

Main characteristics of animal models based on SOD1

It is possible to create transgenic animals (rodents) expressing the human wild-type and mutated SOD1 gene. Currently, transgenic rodents expressing human mutant SOD1 are thought to provide the most suitable animal model of human ALS. There are several lines of transgenic rodents express-ing human mutant SOD1, and their main characteristics
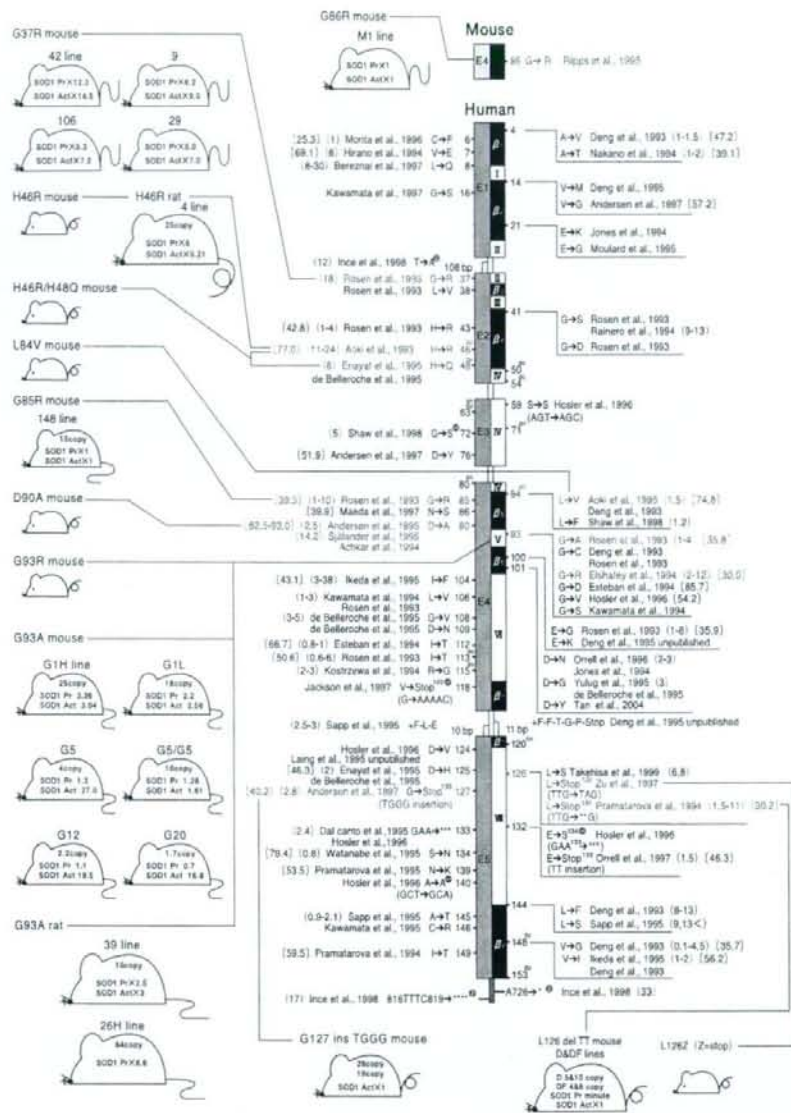
Fig. 2 Schema showing relationship between the main characteristics of transgenic rodents with mutant SOD1 and the main mutation of the human SOD1 gene. The main characteristics of transgenic rodents and human SOD1 gene structure are shown diagrammatically. With respect to transgenic rodents, the main characteristics of copy number, SOD1 protein level (SOD1 Pr), and SOD1 activity (SOD1 Act) in the G93A mouse (lines = G1H, G1L, G5, G5/G5, G12, G20), G37R mouse (lines = 42, 9, 106, 29), G85R mouse (line = 148), G86R mouse (line = M1), L126dellTT mouse (lines = D, DF), G127insTGGG mouse, H46R rat (line = 4), and G93A rat (lines = 39, 26H) are shown within each rodent body; exact values for each unit are described in the text (See "Main characteristics of animal models based on SOD1"). As for the human SOD1 gene structure, *large blue areas* (E1–E5) = exon 1 to 5; *small*

open areas = intron; *small dark gray area* = 3 prime untranslated region. *Large black areas* (beta-sheets) = beta-sheet 1–8; *large open areas* (beta-loops) = beta-loops I to VII [IV, VII = active site; III, VI = Greek key]. Superscript Cu = copper binding site; superscript Zn = zinc binding site; superscript dc = dimer contact. Amino acid or nucleotide substitutions are indicated at appropriate codons according to the accepted international nomenclature. Even SALS has an SOD1 abnormality; each encircled superscript S indicates the SALS. Each encircled superscript N indicates ALS without a familial history. Disease durations (years) are shown in parentheses. FALS shows various disease durations according to the type of SOD1 gene mutation responsible; enzyme activities (% value relative to normal control erythrocytes) are shown in *brackets*. Mouse SOD1 gene structure of exon 4 (E4) is shown in *yellow*

are summarized in this paragraph in detail and shown schematically in Fig. 2. There are six major strains of ALS transgenic rodents carrying human mutant SOD1: G93A mice (lines: G1, G5, G12 and G20) [19–21, 36], G37R mice (lines: 42, 9, 106 and 29) [98], G85R mice (lines: 221, 164, 103, 148, 74, 46, 87 and 124) [10], H46R/H48Q mice (lines:139, 73, 67, and 58) [96], H46R rats (line: 4) [2, 72], and G93A rats (lines: 39) [2, 72] and 26H [43]). In addition, seven types of transgenic mice bearing human mutant SOD1 have been produced: G93R mice [31], D90A mice [49], H46R mice [1], L84V mice [1], L126delTT mice [97], L126Z (Z = stop) mice [23], and G127insTGGG mice [48]. There is a major line of transgenic mice carrying mouse G86R SOD1 (lines: M1, M2 and M3) [81].

With respect to G93A mice [19–21, 36], the original mouse strain G1-G93A carries 18.0 ± 2.6 transgene copy numbers expressing 4.1 ± 0.54 ng human SOD1 protein per μg of total protein (ng human SOD1) with SOD1 activity of 42.6 ± 2.1 U per μg of total protein (U). G5-G93A mice with 4.0 ± 0.6 copies show 1.3 ± 0.21 ng human SOD1 with 27.0 ± 2.9 U SOD1 activity. G12-G93A mice with 2.2 ± 0.8 copies exhibit 1.1 ± 0.22 ng human SOD1 with 19.5 ± 0.8 U SOD1 activity, and G20-G93A mice with 1.7 ± 0.6 copies express 0.7 ± 0.06 ng human SOD1 with 16.9 ± 0.4 U SOD1 activity. The original G1 line differentiates into two sub-lines derived from the same founder. These two sub-lines, named G1H and G1L, express different transgene copy numbers: G1H-G93A mice carrying 25 transgene copy numbers express 3.36 ± 0.84 ng SOD1 protein per μg soluble brain protein (ng SOD/sbp) with SOD1 activity of 3.04 ± 0.71 U per μg sbp (U/sbp), and G1L-G93A mice expressing 18 copies show 2.20 ± 0.9 ng SOD1/sbp with 2.56 ± 0.23 U/sbp SOD1 activity. G5/G5-G93A mice have been newly generated from G5-G93A mice: G5/G5-G93A mice with 10 copies express 1.28 ± 0.44 ng SOD1/sbp with 1.61 ± 0.14 U/sbp SOD1 activity.

With respect to G37R mice [98], the spinal cord tissues of G37R-42 mice express the human SOD1 protein at a level 12.3 times that of the endogenous mouse SOD1 protein with SOD1 activity 14.5 times higher than the control, G37R-9 mice show a 6.2-fold SOD1 protein level in spinal cord tissues and 9.0-fold SOD1 activity relative to the control, G37R-106 mice show a 5.3-fold SOD1 protein level and 7.2-fold SOD1 activity, and G37R-29 mice express a 5.0-fold SOD1 protein level and 7.0-fold SOD1 activity. There is no detailed description of transgene copy numbers in the original literature.

With regard to G85R mice [10], eight lines have been established with transgene copy numbers of 2–15, and lines 221, 164, 103, 148, 74, 87, 124 show a clinical phenotype. The SOD1 protein level (human/mouse) in these lines is 0.5, 0.8, 0.6, 1.0, 0.2, 0.6 and 0.6, respectively. Among

seven lines in G85R mice, G85R-148 mice carrying 15 transgene copies numbers express the same SOD1 activity comparable to the control.

As for G86R mice [81], although there were three original lines of M1, M2 and M3 in G86R mice, only line M3 has not been perpetuated. M1 and M3 show a clinical phenotype, whereas all M2 mice appear phenotypically normal. The M1 line exhibits an equal amount of total SOD1 protein to the control and show almost identical SOD1 activity. Since G86R mice express murine mutant G86R SOD1, they are advantageous for researchers in that the mouse genomic sequence can be used to reproduce the mutation in SOD1.

With regard to transgenic rats with human mutant SOD1, H46R-4 rats carrying 25 transgene copy numbers express human SOD1 protein at 6 times the level of endogenous rat SOD1 and show SOD1 activity in the spinal cord tissues that is 0.21 times the control activity [2, 72]. G93A-39 rats expressing 10 transgene copies express 2.5 times the human SOD1 protein level and show SOD1 activity in spinal cord tissues that is 3 times the control activity [2, 72]. G93A-26H rats with 64 copies express 8.6 times the human SOD1 protein level, and their founder rats (G93A-26HL) with 72 copies show 10.4 times the human SOD1 level [43].

Neurology and neuropathology of animal models based on SOD1

The first report of transgenic mice expressing human mutant SOD1 was published by Gurney et al. [36]. Therefore, these mice—known as Gurney mice—are the most well known and have been used extensively by many researchers. Among these Gurney mice, the G1H- and G1L-G93A strains are the most widely studied [20, 36]. The first clinical symptom of G1H-G93A mice is reportedly a fine tremor in one or more limbs, which appears at approximately 90 to 100 days of age [20]. On the basis of the author's experimental experience with G1H- and G1L-G93A mice, the term "jittering" seems to be a more appropriate descriptor for the early clinical symptoms they show, rather than "tremor". Although spontaneous jittering/tremor as a single sign is not specific as the initial symptom, it is frequently observed in one or both hind legs when motor work loading such as the extension reflex is applied at a very early clinical stage. Many G1H-G93A mice at approximately 100 days of age exhibit clinical symptoms such as slow walking without agility due to muscle weakness, limp tail, jittering/tremor sometimes associated with motor work loading, and incomplete paresis of a single hind limb. These clinical symptoms can be regarded as significant signs of limb paresis and/or muscle weakness. From the author's experience [52, 59], clinical onset in almost all

G1H-G93A mice (B6SJL-TgN[SOD1-G93A]1Gur, JR2726) originating from Jackson Laboratory (Bar Harbor, ME, USA) occurs at about 100 days after birth, and death occurs at approximately 120 days. Neurologically, almost all G1H-G93A mice show a uniform clinical course, beginning with muscle weakness and/or paresis in the hind limbs, followed by ascent of paresis or paralysis to the forelimbs, until by the end stage the mice show severe quadriplegia, lying sideways or in a moribund state.

The essential cytopathological features of transgenic rodents overexpressing human mutant SOD1 are motor neuron loss with astrocytosis, the presence of SOD1-positive inclusions including LBHIs/Ast-HIs, and vacuole formation. Among these three major pathologic features, motor neuron loss with gliosis is the most essential, and is shared between human ALS and human mutant SOD1 transgenic rodents. In the G1H-G93A spinal cord [52, 59], the number of anterior horn cells at 90 days of age is not decreased significantly in comparison with age-matched littermates, whereas neuropil and/or neuronal intracytoplasmic vacuolation is already evident (Fig. 3a). The numbers of anterior horn cells in G1H-G93A mice at 100 days of age are slightly decreased, with abundant vacuoles and few inclusions (Fig. 3b). At 110 days, the mice demonstrate loss of anterior horn cells, some inclusions and vacuole formation. At 120 days, the mice exhibit quadriplegia and/or a moribund state, with severe loss of anterior horn cells and prominent inclusion pathology, although vacuolation pathology is less marked than that at disease onset (Fig. 3c). Although the author has utilized over 200 G1H-G93A mice hitherto and observed that the numbers of anterior horn cells in G1H-G93A mice at 100 days are slightly decreased, a review paper from Bendotti and Carri has indicated that there is 44% loss of motor neurons at 105 days [8]. This difference might be based on variations in the methods used to perpetuate the original G1H-G93A mice among researchers' institutions, the presence or absence of backcross breeding of B6 mice × original G1H-G93A mice, and differences in quantitation methodologies among researchers. Therefore, researchers need to be sufficiently aware of the differences in the genetic background of G1H-G93A mice and research methodologies before drawing conclusions. Clinical onset in most G1L-G93A mice (B6SJL-TgN[SOD1-G93A]1 Gur^dl, JR2300) from Jackson Laboratory occurs at about 185 days after birth, and death occurs after 250 days. G1L-G93A mice examined at 90, 100, 120, and 150 days of age show only vacuolation pathology without significant neuronal loss or inclusion pathology, whereas those aged 180 days reveal slightly decreased numbers of neurons with many vacuoles and a few inclusions. At the terminal stage after 250 days of age, there is significant loss of anterior horn cells, with both inclusion and vacuolation pathologies [52, 59].

Among transgenic rats with human mutant SOD1 [2, 52, 59, 72], H46R line-4 rats develop motor deficits at approximately 145 days of age, whereas G93A line-39 rats show clinical signs at around 125 days. The number of anterior horn cells in H46R rats at 110 days is not significantly decreased in comparison with age-matched littermates. The anterior horn cells of H46R rats at 135 days are slightly decreased in numbers and show inclusions, whereas at 160, 170 and over 180 days, the anterior horn cells are markedly decreased, and show severe inclusion pathology, featuring neuronal LBHIs and Ast-HIs. With respect to G93A rats, the number of anterior horn cells at 70, 90 and 110 days of age is almost the same as that in age-matched littermates, although at 90 and 110 days of age there is marked vacuolation pathology. At 130, 150 and over 180 days of age, there is marked loss of anterior horn cells, along with both inclusion and vacuolation pathology.

Invariably, the core pathology of rodents carrying mutant SOD1 is the lower motor neuron degeneration/death. As far as can be clarified from the original literature, however, the pathological lesions of G93A mice [19–21, 36] are distributed mainly in the spinal cord anterior horn, brainstem motor nuclei, brainstem reticular formation, dorsal motor nucleus of the vagus nerve, red nucleus, interpeduncular nucleus, and substantia nigra. In G37R mice [98], the areas of degeneration are mainly the spinal cord anterior horn, brainstem motor nuclei, and ventral and lateral white matter of the spinal cord. Vacuole formation is also evident in the olfactory bulb, pyriform cortex, striatum, thalamus, hypothalamus, and choroid plexus. G85R mice show severe neuronal abnormalities in the spinal cord ventral motor neurons, including small neurons near the central canal, and rare interneurons of the dorsal horns, as well as brainstem neurons, especially in the pons [10]. G86R mice show a pronounced motor neuron loss within the spinal cord ventral horns [81]. In the brainstem motor neurons, G86R mice show severe motor neuron depletion in the facial nuclei, while the oculomotor and hypoglossal nuclei show less extreme involvement [75]. From a neurochemical viewpoint, G86R mice exhibit vulnerability of the spinal cord motor neurons, which are positive for pNFP, CAT and calretinin proteins [68]. In H46R-4 and G93A-39 rats [2, 72], the central nervous system lesions are located in the spinal cord ventral horns and brainstem motor nuclei, but no pathology is evident in the cerebral cortex and cerebellum. G93A-26H rats are pathologically similar to G93A-39 rats, showing motor neuron loss with prominent vacuolation [43].

Since the pathology of ALS rodents bearing mutant SOD1 is expressed primarily as lower motor neuron degeneration/death, the number of reports describing upper motor neuron pathology in these models is limited in comparison